# Small Signal Analysis of Active Clamp Flyback Converters in Transition Mode and Burst Mode

Pei-Hsin Liu
Texas Instruments
Manchester, NH USA
p-liu@ti.com

***Abstract*—Active clamp flyback (ACF) converters in transition mode improves the full load efficiency of high-frequency AC/DC and DC/DC power supplies with zero-voltage switching (ZVS). To minimize the impact of the circulating energy for ZVS, burst mode control is used to benefit ACF light load efficiency. However, due to the resonance nature of ACF switching current waveforms, it is difficult to characterize the small-signal properties analytically. In this paper, two new small signal models are developed, and analytical design guides are investigated. An average modeling technique for the transition mode ACF is developed which eliminates the complexity of describing the second-order resonance waveforms, and the model enables a higher system bandwidth design. A high-frequency model for burst mode is derived with the describing function method, which identifies the loop compensation impact and differentiates the stability criteria from the conventional ripple-based ($V^2$) control. Enlightened from the models, a novel nonlinear ramp compensation method and a parallel damping technique are proposed to improve the loop stability and optimize the dynamic response. Finally, SIMPLIS simulations verify the model accuracy, and the fast transient response with the compensation methods are demonstrated on a high-density 45W GaN ACF notebook adapter.**

***Keywords—Active clamp Flyback; transition mode; burst mode; small signal model; ramp compensation***

## I. INTRODUCTION

Active clamp flyback converter (ACF) provides greater efficiency at a higher switching frequency ($f_{SW}$) than the conventional flyback converters, because of zero voltage switching (ZVS) and recycling the leakage energy of the transformer to output [1][2][3]. Besides, the transition mode (TM) operation obtains ZVS across a wider operating range than the continuous conduction mode (CCM) by fully utilizing the magnetizing energy of the transformer [4][5][6]. As the high-side switch ($Q_H$) of ACF conducts, the magnetizing current ($I_M$) can change in a reverse direction in TM. After $Q_H$ turns off, the negative magnetizing current ($I_{M(-)}$) is used to discharge the switch-node capacitance ($C_{SW}$), so the switch-node voltage ($V_{SW}$) can transient to 0V before $Q_L$ turns on. Even though the widely used constant-frequency peak current control may allow ACF running in TM at a higher input bulk-capacitor voltage ($V_{BULK}$) conditions, the efficiency at a lower $V_{BULK}$ and/or a lower output voltage ($V_O$) conditions impairs due to losing $I_{M(-)}$ in CCM. Moreover, the subharmonic oscillation issue and the phase delay effect of right-half-plane (RHP) zero in CCM complicates the control loop designs and limits the outer-loop control bandwidth [7].

Instead, the variable-frequency hysteresis current-mode control of UCC28780 resolves those issues, since the additional emulated valley current loop independently controls $I_{M(-)}$ to prevent ACF from entering into CCM. The block diagram and switching waveforms are illustrated in Fig. 1 [8]. The peak current loop controls the peak magnetizing current ($I_{M(+)}$) sensed from the current sense resistor ($R_{CS}$), and the valley current loop indirectly controls $I_{M(-)}$ by an adaptive ZVS control loop inside the controller. The loop identifies the ZVS condition on $V_{SW}$ every cycle to auto-tune the on time width of $Q_H$. However, the second-order resonance waveform of ACF makes the small-signal modeling very difficult. So far, only two complex mathematical models for voltage-mode controlled ACF were discussed, a numerical approach in [9][10] and a high-order average model in [11], so the analytical model for a current-mode controlled ACF still needs further investigation.

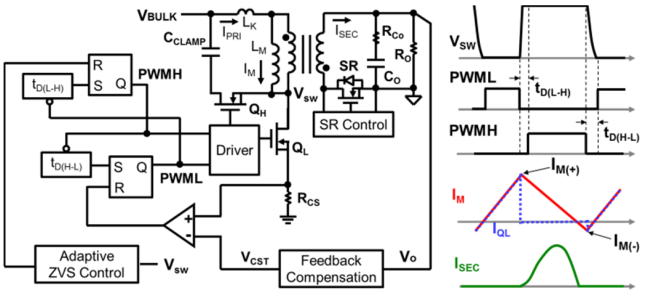


Fig. 1. Hysteresis current mode control of UCC28780 for TM ACF [8]

Once the output load reduces, the light load efficiency becomes very sensitive to the circulating energy needed for ZVS. When the peak current loop reduces $I_{M(+)}$ to regulate the output power, $I_{M(+)}$ and $I_{M(-)}$ become comparable in light load. The increased contribution of the circulating energy impairs the transformer efficiency. The burst mode control improves ACF efficiency, since the ratio of $I_{M(+)}$ and $I_{M(-)}$ of each switching cycle in a burst packet can remain higher [12]. The block diagram and operation waveforms of the burst mode control in UCC28780 are shown in Fig. 2. Since $I_{M(+)}$ is clamped by a fixed peak current threshold ($V_{CST}$), $V_O$ regulation is achieved by using a ripple regulator to compare the $V_O$ feedback signal ($V_{FB}$) with the sum of a reference voltage ($V_{REF}$) and a clean compensation ramp ($V_{COMP}$) [8]. $V_{COMP}$ can be used to mitigate the interference of noisy $V_{FB}$ content onto the intersection point change in steady state. The regulator output (RUN) goes high to initiate the next burst cycle when the two signals intersect. The counter limits the maximum number of switching cycles in a burst packet by resetting the RUN signal.

As illustrated in Fig. 2, when ACF stops switching during the burst off time, $V_O$ ripple and $V_{FB}$ ripple are linearly reduced because the output capacitor voltage is discharged by the output load. When $V_{FB}$ becomes lower than the sum of $V_{REF}$ and $V_{COMP}$, a group of switching pulses are generated to charge the output capacitor, so $V_O$ ripple and $V_{FB}$ ripple increase. The output filter configuration influences the shape of $V_{FB}$ ripple, so it is critical to understand how the equivalent series resistance (ESR) of the output capacitor and the π output filter affect the burst loop stability. For the conventional ripple-based control ($V^2$ control) modulated by the switching frequency ripple, it is found that when the ESR ripple ($\Delta V_{Rco}$) of the low-ESR output capacitor is overwhelmed by the capacitor voltage ripple ($\Delta V_{Co}$), the phase delay between $\Delta V_{Co}$ and the switching current ripple of a $V^2$ controlled Buck converter caused subharmonic oscillation [13][14]. On the other hand, for the burst mode control modulated by the burst frequency ripple, $\Delta V_{Co}$ is like a triangular waveform, but not like the sinusoidal waveform in $V^2$ control, so the small-signal property needs further investigation and detail comparison.

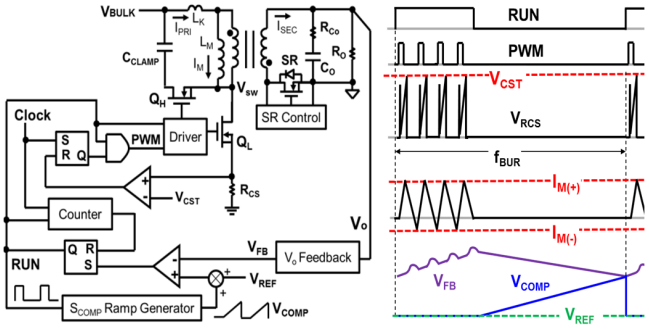


Fig. 2. Burst mode control of UCC28780 [8]

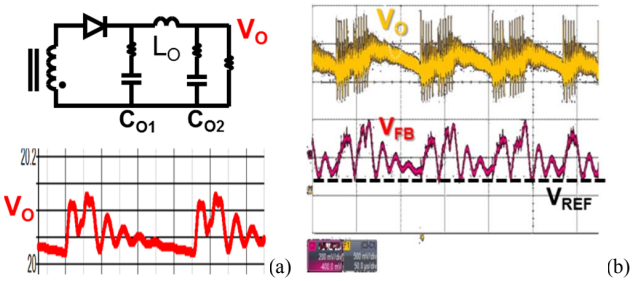


Fig. 3. ACF with a π filter in burst mode: (b) with $V_{COMP}$, (b) without $V_{COMP}$

Besides, Fig. 3 (a) shows the simulation result of $V_O$ ripple from the burst mode controlled ACF with a π output filter, when $V_{COMP}$ is properly designed. Compared with Fig. 2 with a single output capacitor, there is an additional ringing superimposed on the output ripple in burst off time, generated from the resonance between the output inductor ($L_O$) and the filter capacitor ($C_{O1}$). Without $V_{COMP}$, the additional ringing on the falling slope of $V_{FB}$ can very easily reach $V_{REF}$. Then, the next burst packet may be prematurely triggered, so the adjacent burst packets may group together as shown in Fig. 3 (b). The grouping packets cause loud audible noise, and increases output voltage ripple. To resolve this, it is very critical to push the undesirable ripple content of $V_{FB}$ away from $V_{REF}$ by designing a larger $V_{COMP}$. Therefore, how to reduce the tradeoff on the transient response or how to design $V_{COMP}$ requires more detail analysis.

This paper introduces two new small signal models for the hysteresis current mode controlled ACF in transition mode and burst mode operations respectively, and provides detailed design guidelines for optimizing the loop compensation based on the derived models. In Section II, the proposed modeling approach for the transition mode ACF is explained, a simple equivalent circuit representation is proposed for an intuitive understanding of the current mode controlled ACF, and the model is extended to analyze the parallel damping design for ACF with a π output filter. In Section III, the high-frequency modeling approach for the burst control loop is introduced, $V_{COMP}$ effect on the dynamic response is analyzed, and the distinctive small-signal property is compared with $V^2$ control. In Section IV, a passive ripple compensator for a stable burst operation and a nonlinear ramp compensation method to improve the transient response are described. In Section V, the simulation and experimental results verify the effectiveness of the compensation techniques.

## II. Small-Signal Model in Transition Mode

### A. Proposed Average Model for ACF in Transition Mode

The key steps of the proposed modeling procedure for transition-mode ACF are described as follows. Firstly, based on the triangular approximation on the magnetizing current in [12], an analytical form for the average value of the switching current waveform on $Q_L$ ($I_{QL}$) can be derived as:

$$I_{QL} \approx \frac{1}{2}\left(\frac{V_{CST}}{R_{CS}} + I_{M(-)}\right)\frac{N_{PS}V_O}{V_{BULK} + N_{PS}V_O} \quad (1)$$

where $V_{CST}$ is the peak current threshold of the peak current control loop, $R_{CS}$ is the sensing resistor in series with $Q_L$, $V_{BULK}$ is the input voltage, $N_{PS}$ is the turn ratio between primary and secondary windings, and $V_O$ is the output voltage. Secondly, since ACF input current is equal to $I_{QL}$, the average value of $I_{SEC}$ can be easily obtained from the energy conservation law with a given power stage efficiency (ƞ), which is $(V_{BULK}\cdot I_{QL})\cdot ƞ/V_O$. This simple averaging technique avoids the complication on describing the resonance waveform of the secondary side. Thirdly, $I_{SEC}$ is linearized around its operating point by calculating the partial derivatives to $\hat{v}_{CST}$, $\hat{v}_{BULK}$ and $\hat{v}_O$ perturbations.

$$\hat{i}_{SEC} = K_E\hat{v}_{CST} + K_F\hat{v}_{BULK} + K_R\hat{v}_O \quad (2)$$

where $K_E = \partial I_{SEC}/\partial V_{CST}$, $K_F = \partial I_{SEC}/\partial V_{BULK}$, and $K_R = \partial I_{SEC}/\partial V_O$, all of which are summarized in Table 1. The parameters in Table 1 are written as a function of $V_{CST}$, $V_{BULK}$, and $V_O$. The $I_{m(-)}$ expression in Table 1 is valid only when the dead time setting for the $V_{SW}$ falling edge, $T_{D(H-L)}$, is designed based on the state trajectory for ZVS [1].

Fourthly, the three derivation terms in superposition can be represented as the equivalent circuit model in Fig. 4. The first two terms in (2) are modeled as the two voltage-controlled current sources, modulated by $\hat{v}_{CST}$ and $\hat{v}_{BULK}$ respectively. The third term in (2) is equivalent to the internal resistance

($R_E$) of the two non-ideal current sources. Finally, the $v_{CST}$-to-$v_O$ transfer function under $\hat{v}_{BULK}$=0V is derived as:

$$\frac{v_O(s)}{v_{CST}(s)} = \frac{K_E(R_E // R_O)(1+sC_oR_{Co})}{1+sC_o[(R_E // R_O)+R_{Co}]} \quad (3)$$

where the positive resistance $R_E$ is -1/$K_R$, $R_O$ is the output load resistance, $R_{Co}$ is the output capacitor ESR, and $C_O$ is the capacitance of the output capacitor.

Fig. 5 compares the Bode plot of the transfer function with the SIMPLIS simulation result on a 45W ACF design at both high line and low line cases. The ACF power stage parameters are $L_K$=1μH, $L_M$=57μH, $N_{PS}$=4.292, $C_{SW}$=103pF, $C_{CLAMP}$=86nF, $R_{CS}$=0.205Ω, $V_{CST}$=0.356V, and a single output capacitor with $R_{Co}$=10mΩ and $C_O$=330μF. The simulation condition for $V_{BULK}$=325V and $V_{BULK}$=70V cases is $V_O$=20V and $I_O$=2.25A. The model matches with the simulation result up to one fifth of switching frequency. This accuracy is useful enough for the practical bandwidth target of the offline power supply. The discrepancy close to $f_{SW}$/2 is generated by the inability to capture the current loop delay effect of the side-band frequency components, which is the natural limitation of the averaging modeling addressed in [13][15][19]. Finally, this model can easily extend to other soft-switching flyback converters in [16] as well.

TABLE I. PARAMETERS FOR THE ACF EQUIVALENT CIRCUIT MODEL

| | |
|---|---|
| $I_{M(-)}$ | $-V_{BULK}\sqrt{C_{SW}/L_M}$ for $V_{BULK} > N_{PS}V_O$<br>$-N_{PS}V_O\sqrt{C_{SW}/L_M}$ for $V_{BULK} < N_{PS}V_O$ |
| $K_E$ | $N_{PS}V_{BULK}/[2R_{CS}(V_{BULK}+N_{PS}V_O)]$ |
| $K_R$ | $-\frac{N_{PS}^2V_{BULK}(V_{CST}+R_{CS}I_{M(-)})}{2R_{CS}(V_{BULK}+N_{PS}V_O)^2}$ |
| $V_{CST}$ | $\frac{2P_{IN}(V_{BULK}+N_{PS}V_O)-N_{PS}V_OV_{BULK}I_{M(-)}}{N_{PS}V_OV_{BULK}}R_{CS}$ |
| $K_F$ | $\frac{N_{PS}^2V_OV_{CST}+N_{PS}I_{M(-)}R_{CS}(V_{BULK}+2N_{PS}V_O)}{2R_{CS}(V_{BULK}+N_{PS}V_O)^2}$ |

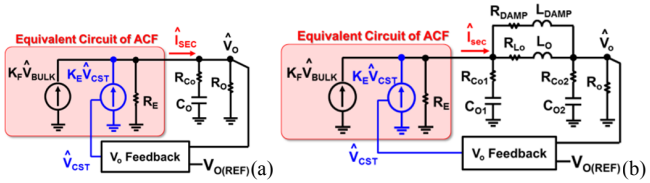


Fig. 4. Equivalent circuit model for ACF in transition mode: (a) with a single output capacitor, (b) with a π filter and a parallel damping network

## B. Damping the Double Pole of ACF with a π Output Filter

A π output filter for ACF not only helps to reduce the $V_O$ ripple magnitude, but also improves ACF full-load efficiency over 1%, because the slightly discharged $C_{O1}$ voltage by the output load during $Q_L$ on time helps to attract more magnetizing current to the secondary winding after $Q_L$ turns off, and results in the conduction loss reduction of $Q_H$ and the primary winding [1][6]. If the $V_O$ feedback point is the $C_{O1}$ terminal voltage, the compensator gain may need to be reduced greatly to overcome the large $C_{O1}$ voltage ripple effect on $V_{FB}$, so the loop bandwidth is compromised. Instead, if the feedback point is the $C_{O2}$ terminal voltage, the $L_O$ and $C_{O1}$ double pole peaking may cause a second crossover on the loop gain, so it becomes another limitation on a higher control loop bandwidth design.

Therefore, a simple parallel damping network ($R_{DAMP}$ and $L_{DAMP}$) with $L_O$ is proposed to damp the double pole peaking and enable a higher bandwidth design. Compared with the shunt damping network with $C_{O1}$ in [17], the parallel damping provides less impact on the resonance period between the reflected leakage inductance and $C_{O1}$, so the resonance current waveform of ACF and the winding loss will not be influenced. The damping network design in frequency domain can also be developed based on the proposed equivalent circuit model in Fig. 4(b). From the $v_{CST}$-to-$v_O$ transfer function, the damping factor (ζ) of the double pole is calculated as:

$$\zeta \approx \frac{1}{2}\frac{R_{DAMP}}{1+K_{DAMP}}\sqrt{\frac{C_{O1}}{L_O}} \quad (4)$$

where $K_{DAMP}$ is $L_{DAMP}/L_O$. Based on [18], the optimal damping factor ($\zeta_{OPT}$) with minimum double pole peaking is:

$$\zeta_{OPT} = \sqrt{\frac{K_{DAMP}(3+4\cdot K_{DAMP})(1+2\cdot K_{DAMP})}{2(1+4\cdot K_{DAMP})}} \quad (5)$$

Combining the two equations and defining $R_{DAMP}=\sqrt{L_O/C_{O1}}$, it is found that $K_{DAMP}$ of 0.13 obtains minimum peaking.

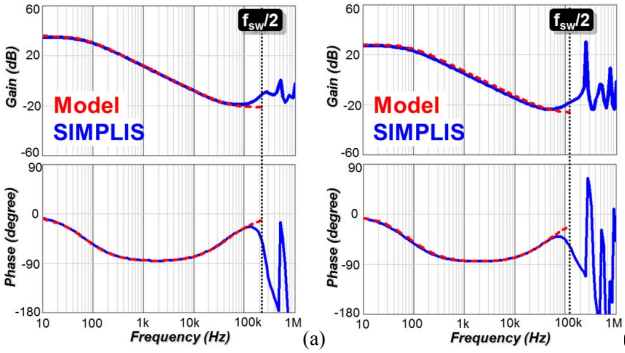


Fig. 5. TM model verification in SIMPLIS: (a) $V_{BULK}$=375V, (b) $V_{BULK}$=70V

# III. SMALL-SIGNAL MODEL IN BURST MODE

## A. Proposed High Frequency Model for ACF in Burst Mode

Since the burst mode control in Fig. 2 is modulated with the $V_{FB}$ burst ripple, the above average modeling technique is inadequate to characterize the dynamic of the side-band components of the perturbed $v_{FB}$ spectrum. Therefore, this paper applies the describing function method in [19] to model the burst control loop as a single entity to capture the key side-band contributions. The concept is that a small sinusoidal signal with a perturbation frequency of $f_m$ is injected to $v_{REF}$, and the perturbed $v_{FB}$ waveform in Fig. 6 is described mathematically, so $v_{REF}$-to-$v_{FB}$ transfer function can be derived based on calculating the Fourier coefficient at $f_m$. The assumptions and derivation steps are same as [19]. Therefore, only critical steps are listed in this paper.

Firstly, because the switching period ($T_{SW}$) of each switching cycle and the number of switching pulses ($N_{SW}$) in a burst packet are fixed, only the burst off-time ($T_{OFF}$) is modulated by the perturbation signal $v_{REF}(t) : v_{REF}(t) = V_{REF} + \hat{r} \cdot \sin(2\pi f_m t + \theta)$, where $V_{REF}$ is the DC reference of the ripple comparator, $\hat{r}$ is the perturbation magnitude, and $\theta$ is the initial angle. Based on the modulation law, it is found that:

$$\begin{aligned} &v_{REF}(t_{i-1} + T_{OFF(i-1)}) + S_{COMP} T_{OFF(i-1)} + S_N N_{SW} T_{SW} \\ &= v_{REF}(t_i + T_{OFF(i)}) + (S_{COMP} + S_F) T_{OFF(i)} \end{aligned} \quad (6)$$

where $T_{OFF(i)}$ is the perturbed off time of $i_{th}$ bust cycle, $S_{COMP}$ is the rising slope of the compensation ramp $V_{COMP}$, $S_F$ is the falling slope of the $V_{FB}$ burst ripple, and $S_N$ is the linear approximation on the rising slope of $V_{FB}$ burst ripple. The approximation is based on the assumption that when the period of a burst cycle ($T_{BUR}$) is much longer than $T_{SW}$ in a burst packet, the influence of the high-frequency switching ripple content to the intersection point is negligible. Besides, since ACF is not switching in $T_{OFF}$, output load current ($I_O$) discharges the output capacitor voltage, and $S_F$ of $V_{FB}$ is proportional to $I_O/C_O$. Assuming $T_{OFF(i)} = T_{OFF} + \Delta T_{OFF(i)}$, (6) can be simplified as:

$$(S_{COMP} + S_F)\Delta T_{OFF(i)} - S_{COMP}\Delta T_{OFF(i-1)} = v_{REF}(t_{i-1} + T_{OFF(i-1)}) - v_{REF}(t_i + T_{OFF(i)}) \quad (7)$$

where $S_N$ is cancelled out because the fixed $N_{SW}$ and $T_{SW}$ of the adjacent burst packets make $S_N$ the same.

Secondly, the perturbed burst duty cycle $d_{BUR}(t)$ and the perturbed secondary-winding current $i_{SEC}(t)$ can be expressed by (8) and (9) respectively:

$$d_{BUR}(t) = \sum_{i=1}^{M} [u(t - t_i - T_{OFF(i)}) - u(t - t_i - T_{OFF(i)} - N_{SW} T_{SW})] \quad (8)$$

$$i_{SEC}(t) \approx \frac{T_{BUR} I_O}{N_{SW} T_{SW}} d_{BUR}(t) \quad (9)$$

where u(t)=1 when t>0, and $T_{BUR}=N_{SW}T_{SW}+T_{OFF}$. Then, the Fourier analysis can be performed on $i_{SEC}(t)$ as:

$$c_{m(i_{SEC})} = j\frac{2 f_m}{N} \int_0^{t_M + T_{OFF(M)} + N_{SW} T_{SW}} i_{SEC}(t) \cdot e^{-j2\pi f_m t} dt \quad (10)$$

where $c_{m(iSEC)}$ is the Fourier coefficient at the perturbation frequency $f_m$ for the secondary-winding current. Based on the same step in [19], the coefficient is calculated as:

$$c_{m(i_{SEC})} = \hat{r} \frac{1 - e^{-j2\pi f_m (N_{SW} T_{SW})}}{(S_{COMP} + S_F) - S_{COMP} e^{-j2\pi f_m T_{BUR}}} \frac{I_O}{N_{SW} T_{SW}} e^{-j\theta} \quad (11)$$

Thirdly, when the $V_o$ feedback network can be simplified as the proportional feedback gain of $K_{FB}$, $S_F$ of $V_{FB}$ is equal to $K_{FB}I_O/C_O$, and the Fourier coefficient of $v_{FB}$, $c_{m(VFB)}$, can be expressed by:

$$C_{m(v_{FB})} = K_{FB} C_{m(i_{SEC})} \frac{(R_{Co} C_o \cdot j2\pi f_m + 1)}{C_o \cdot j2\pi f_m} \quad (12)$$

Fourthly, the Fourier coefficient at the perturbation frequency $f_m$ for the reference signal $v_{REF}(t)$ is $\hat{r}e^{-j\theta}$, so the describing function from $v_{REF}$ to $v_{FB}$ in s domain can be calculated as:

$$\frac{v_{FB}(s)}{v_{REF}(s)} = \frac{(1 - e^{-s(N_{SW} T_{SW})})(1 + s \cdot R_{Co} C_o)}{(S_{COMP} + S_F) - S_{COMP} e^{-sT_{BUR}}} \frac{S_F}{s \cdot N_{SW} T_{SW}} \quad (13)$$

After that, the Pade' approximation is used to simplify the exponential terms of (13) into a reduced-order transfer function, valid up to half of the burst frequency ($f_{BUR}$):

$$\frac{v_{FB}(s)}{v_{REF}(s)} \approx \frac{1 + s \cdot R_{Co} C_o}{1 + s \cdot (\frac{S_{COMP}}{S_F} + \frac{1}{2}) T_{BUR} + s^2 \frac{T_{BUR}^2}{\pi^2}} \frac{1 + s\frac{T_{BUR}}{2} + s^2 \frac{T_{BUR}^2}{\pi^2}}{1 + s\frac{N_{SW} T_{SW}}{2} + s^2 \frac{N_{SW}^2 T_{SW}^2}{\pi^2}} \quad (14)$$

Finally, the first-order approximation is applied to further simplify (14) for understanding the physical meaning easier:

$$\frac{v_{FB}(s)}{v_{REF}(s)} \approx \frac{1 + s \cdot R_{Co} C_o}{1 + s \cdot (\frac{S_{COMP}}{S_F} + \frac{1}{2}) T_{BUR}} \cdot \frac{1 + s\frac{T_{BUR}}{2}}{1 + s\frac{N_{SW} T_{SW}}{2}} \quad (15)$$

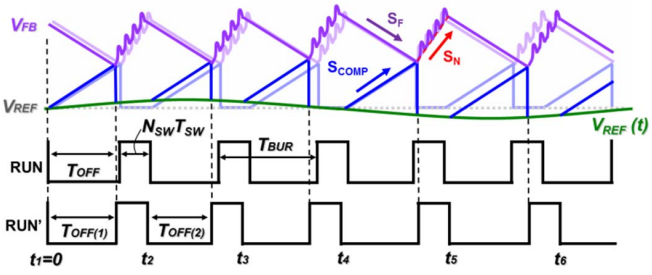


Fig. 6. $v_{FB}$ waveform under a small sinusoidal perturbation of $v_{REF}$

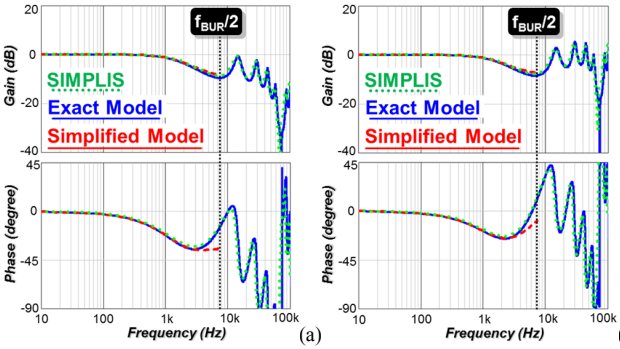


Fig. 7. Burst model verification in SIMPLIS: (a) $R_{Co}$=2mΩ, (b) $R_{Co}$=20mΩ

Fig. 7 shows the Bode plot comparison between the SIMPLIS simulation and proposed model to verify the accuracy under two different ESR values of the output capacitor. The ACF power stage parameters are $L_K$=1μH, $L_M$=100μH, $N_{PS}$=4.292, $C_{SW}$=103pF, $C_{CLAMP}$=200nF, $R_{CS}$=0.157Ω, $V_{CST}$=0.3V, and a 600μF output capacitor with $R_{Co}$=2mΩ or 20mΩ. The simulation conditions are $V_{BULK}$=375V, $V_O$=20V, $N_{SW}$=4, and $I_O$=0.5A. The results indicate that the exact model with exponential terms in (13) is well matched with the SIMPLIS simulation beyond $f_{BUR}/2$, while the simplified model in (15) provides good enough accuracy to $f_{BUR}/2$. Besides, the results prove that the loop stability of the burst mode control is insensitive to the output

capacitor selection. Even though the burst mode control does not need $S_{COMP}$ from the loop stability aspect, $V_{FB}$ burst ripple with a low-ESR output capacitor may be too small under small $K_{FB}$, so the background noise may prematurely trigger next burst cycle, and cause inconsistent burst frequency variation. In practice, $S_{COMP}$ is still needed to improve the signal to noise ratio of the ripple comparator.

### *B. Comparison with Conventional Ripple-based ($V^2$) Control*

Proposed model provides two new insights on the small-signal property of the burst mode control. Firstly, the low-frequency dominate pole characterizes the $S_{COMP}$ impact on the loop response. When $S_{COMP}$ increases in a given output load condition, the dominate pole will move to a lower frequency and reduce the gain of the transfer function, so the transient response will be compromised. Besides, the model indicates that a fixed linear $S_{COMP}$ design significantly impairs the transient response in lighter load, since $S_F$ slope reduces with output load and makes the dominate pole moved to even lower frequency. Secondly, the expression of the high-frequency double poles in (14) indicates that the burst mode control is inherently stable even with a low-ESR output capacitor, assuming the $V_{FB}$ ripple reflects the $V_O$ burst ripple. On the other hand, the conventional ripple based control ($V^2$ control) modulates the switching ripple, so the delay effect of the capacitor voltage ripple can cause the subharmonic oscillation. The model of constant on-time $V^2$ control contains a double pole at $f_{SW}/2$ and will move in the right half plane, when a low-ESR capacitor is used [13][14].

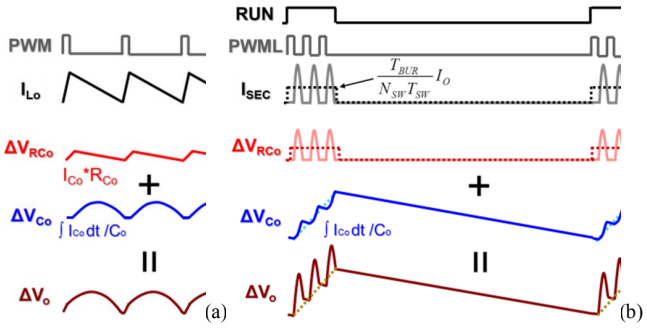


Fig. 8. Output ripple breakdown: (a) constant on-time $V^2$ control for a Buck converter, (b) burst mode control for ACF

Another way to understand the difference on the small-signal property between the $V^2$ control and the burst control more intuitively comes from the output ripple breakdown. For a constant on-time $V^2$ controlled Buck converter as an example, the perturbed switching node voltage by the modulation signal is a pulse waveform, while the perturbed switching current flowing through the Buck inductor is the integration of the voltage difference between the switch-node voltage and output voltage. Then, the ESR ripple voltage of the output capacitor ($\Delta V_{Rco}$) is in-phase with the Buck inductor current, and the capacitor ripple voltage ($\Delta V_{Co}$) is the integration of the Buck inductor current. As shown in Fig. 8(a), there is a -90° phase shift between $\Delta V_{Rco}$ and the PWM signal in frequency domain due to the integration of Buck inductor, while there is -180° phase shift between $\Delta V_{Co}$ and the PWM signal due to both the integration of the Buck inductor and the integration of the output capacitor. Conceptually, when $\Delta V_{Co}$ contribution is stronger for a low-ESR output capacitor, the stability issue may occur, and the double pole expression in [13][14] reflects the $\Delta V_{Co}$ contribution with the -180° phase shift.

On the other hand, for a burst mode controlled switching converter, grouped switching current waveforms in a burst packet can be treated as a pulse burst current waveform in low-frequency approximation. Then, when the burst period is perturbed by the modulation signal, the perturbed burst current waveform is in phase with the RUN signal in the frequency domain. As shown in Fig. 8(b), when the current flows to the output capacitor, $\Delta V_{Rco}$ is still in phase with the RUN signal, while there is -90° phase shift between $\Delta V_{Co}$ and the RUN signal due to the integration effect from the output capacitor. Conceptually, because of no -180° phase shift on $\Delta V_{Co}$, the stability issue disappears, which agrees with the double pole expression in (14).

## IV. Proposed Loop Compensation for Burst Mode

Fig. 9 shows the proposed compensation network for burst-mode controlled isolated converters, and is not limited to ACF only. First is the passive ripple compensator, $R_{DIFF}$ and $C_{DIFF}$ in parallel with the opto-coupler bias resistor ($R_{BIAS}$), which compensates the phase delay of the opto-coupler, so $I_{OPTO}$ and $V_{FB+COMP}$ can recover $V_O$ burst ripple. Due to the miller effect of collector-to-base capacitance of the BJT in the opto-coupler output, the collector-to-emitter capacitance and the pull-up resistance of the current mirror introduces a very low frequency single pole. The compensation zero from $R_{DIFF}$+$R_{BIAS}$ and $C_{DIFF}$ should be positioned close to the single pole. Second is the active ripple compensator, $R_{COMP}$ and a small-signal MOSFET ($Q_{COMP}$), which generates a nonlinear $S_{COMP}$ ramp slope to reduce the noise sensitivity of the ripple regulator without sacrificing the transient response of ACF.

Even though a sharper linear $S_{COMP}$ makes the burst control loop less noise sensitive, the issue is the slower dynamic response, since (15) indicates that a sharper $S_{COMP}$ moves the dominate pole to a lower frequency and the load-dependent $S_F$ further aggravates the issue. On the other hand, the proposed nonlinear $S_{COMP}$ slope generator in Fig. 9 behaves like a sharp slope at the beginning of burst off time to push the noisy $V_{FB+COMP}$ away from $V_{REF}$, so the next burst cycle will not be triggered prematurely by the noisy ripple content of ACF, such as the $L_O$ and $C_{O1}$ resonance ripple of the π filter or the switching noise. When $T_{BUR}$ becomes longer with a lighter output load, the nonlinear ramp slope is gradually reduced, so the transient response can be greatly improved with a shallow $S_{COMP}$ around the intersection point.

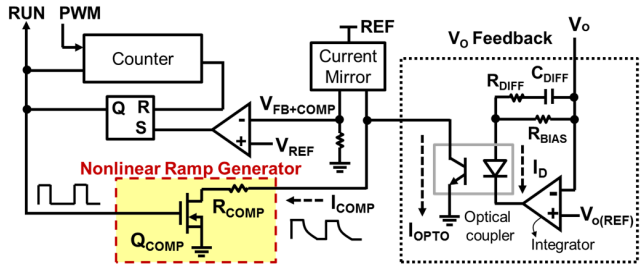


Fig. 9. Proposed loop compensation network for burst mode control

In the example circuit implementation, when $Q_{COMP}$ is ON as RUN is high, $R_{COMP}$ can adjust the offset amplitude of compensation current ($I_{COMP}$). Next, when $Q_{COMP}$ is OFF as RUN is low, the time constant of $R_{COMP}$ and the junction capacitance of $Q_{COMP}$ ($C_{OSS(Qcomp)}$) determines the falling slope of $I_{COMP}$. $S_{COMP}$ on $V_{FB+COMP}$ in this circuit can be calculated as

$$S_{COMP}(T_{BUR}) = \frac{K_{COMP}V_{REF}}{R_{COMP}C_{OSS(Qcomp)}} e^{\frac{-(T_{BUR}-N_{SW}T_{SW})}{R_{COMP}C_{OSS(Qcomp)}}} \quad (16)$$

where $K_{COMP}$ is the product of the current mirror gain and the internal resistor between $V_{FB+COMP}$ and ground.

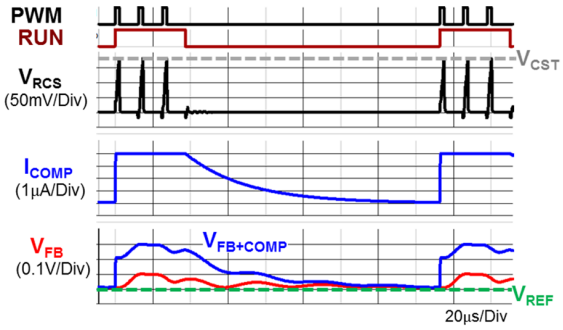


Fig. 10. Operation principle of proposed compensation network

## V. Experimental and Simulation Verifications

The high-density ACF hardware to support the study of the paper is shown in Fig. 11, which is also the evaluation board of UCC28780 ACF controller. On the GaN-based ACF hardware, two 650V GaN power IC (NV6115 and NV6117) from Navitas Semiconductor are used as the two primary-side switches. UCC24612 controller is selected to drive the 150V MOSFET as the synchronous rectifier. The ACF power stage parameters are $L_K$=2.5μH, $L_M$=115μH, $N_{PS}$=5.25, $R_{CS}$=0.227Ω, $C_{CLAMP}$=440nF (ceramic), $C_{O1}$=66μF (ceramic), $L_O$=1μH, $C_{O2}$=680μF (polymer), and $R_{Co2}$=20mΩ.


Fig. 11. UCC28780 evaluation board as the GaN-based ACF hardware

### A. Parallel Damping Effect for ACF in Transition Mode

From the small-signal analysis, $L_{DAMP}$=0.13·$L_O$ provides strongest damping on the double pole peaking of $L_O$ and $C_{O1}$. However, too strong damping will cause more AC current flowing through the damping network and introduce more power loss at full load. When $L_{DAMP}$ is 0.15μH and $L_O$ is 1μH, the full load efficiency at 90Vac drops 0.5% compared with no $L_{DAMP}$. On the other hand, if $L_{DAMP}$>0.13·$L_O$, less AC current flows through the network and results in less power loss. When $L_{DAMP}$ is 0.68μH and $L_O$ is 1μH, the full load efficiency at 90Vac drops only 0.15% compared with no $L_{DAMP}$. The loop gain test results of the hardware are shown in Fig. 12, and the test condition is at $V_{BULK}$=375V, $V_O$=20V, and $I_O$=2.25A. For ACF with a single output capacitor ($L_{DAMP}$ is open), the first order plant characteristic provides enough phase margin when the control bandwidth is pushed to 5kHz, as shown in Fig. 12(a). For ACF with the π output filter, the result in Fig. 12(b) indicates that proposed damping is able to prevent the second crossover on the loop gain compared with no $L_{DAMP}$, so the damping technique enables a higher system bandwidth design for ACF with a π output filter. Fig. 13 compares the difference of the resonance current waveform on the primary winding ($I_{PRI}$), when the parallel damping is applied. The test result indicates that there is no significant difference on the resonance period and the RMS value, so the transformer loss attribution will not be affected by the damping network.

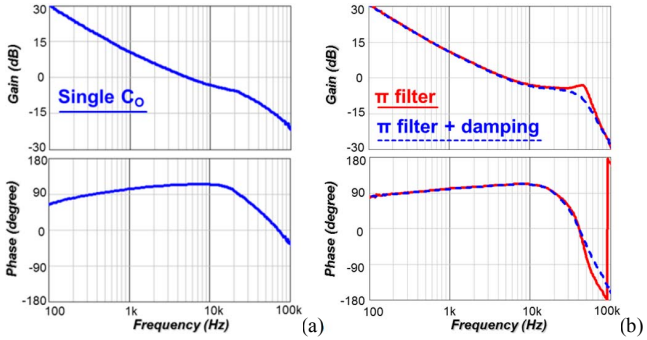


Fig. 12. Loop gain test: (a) ACF with a single output capacitor, (b) damping effect on the ACF with a π output filter

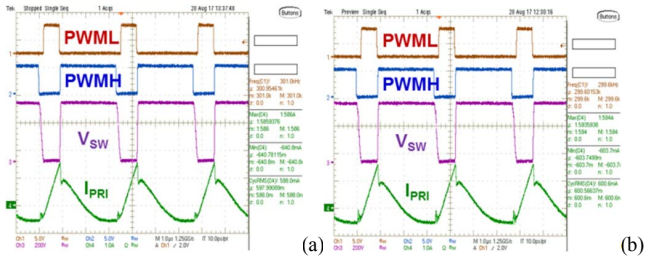


Fig. 13. ACF resonance waveforms: (a) no damping, (b) with damping

### B. Proposed Loop Compensation Method and Parallel Damping Effect for ACF in Burst Mode

The test condition of the following results is at $V_{BULK}$=120V, $V_O$=20V, and $I_O$=0.5A. Based on proposed guidelines for $R_{COMP}$ and $C_{COMP}$, the feedback current ($I_{OPTO}$) in Fig.14 is able to recover the output burst-frequency ripple on the primary feedback loop. $I_{OPTO}$ waveform is measured by the voltage across a 2kΩ resistor in series with the opto-coupler. The result is tested with a single output capacitor, and the consistent burst operation is obtained with the proposed passive ripple compensator. Besides, when a π output filter is used, the $L_O$ and $C_{O1}$ resonance ripple prematurely triggers the next burst cycle and results in the group pulse effect, as shown in Fig. 15(a). After the proposed nonlinear ramp compensation is applied in conjunction with the parallel damping, the consistent burst packet is obtained, as shown in Fig. 15(b). The system-level benefits are to eliminate the audible noise and reduce the peak-to-peak output ripple in burst operation.

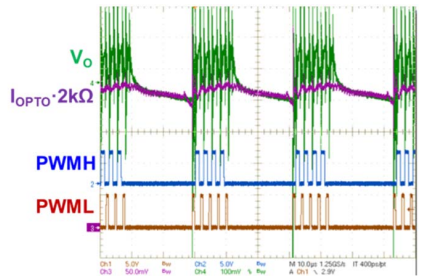


Fig. 14. $V_O$ and $I_{OPTO}$ waveforms with the passive ripple compensator for ACF with a single output capacitor

The benefit of the parallel damping for burst mode is to obtain more consistent switching current waveforms and the SR MOSFET operation in each switching cycle. Fig. 16(a) shows that even though the burst frequency is stable with nonlinear $S_{COMP}$, the underdamped output filter creates a large voltage ripple on $C_{O1}$ terminal, so the larger time-variant voltage difference between the $C_{CLAMP}$ voltage and the reflected $C_{O1}$ voltage causes the redistribution of the magnetizing current between primary and secondary windings and results in SR prematurely turnoff in some switching cycles. As shown in Fig. 16(b), when the parallel damping is applied, the $C_{O1}$ ripple voltage is reduced greatly, so the winding current and the SR operation becomes more consistent among switching cycles.

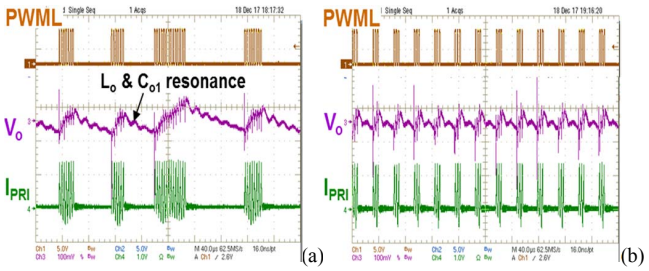


Fig. 15. Burst mode operation for ACF with a π output filter: (a) no $S_{COMP}$, (b) with nonlinear $S_{COMP}$

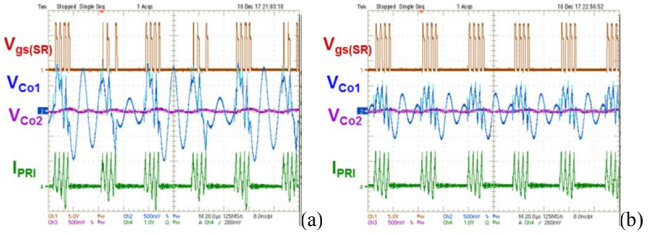


Fig. 16. Burst mode with nonlinear $S_{COMP}$ for ACF with a π output filter: (a) no parallel damping, (b) with parallel damping

### C. *Transient Response of Burst Mode with Nonlinear $S_{COMP}$*

The simulation Bode plots of $v_{REF}$-to-$v_O$ transfer function for the burst mode controlled ACF using the conventional linear $S_{COMP}$ and the proposed nonlinear $S_{COMP}$ are compared in Fig. 17. The ACF power stage parameters are $L_K$=1μH, $L_M$=100μH, $N_{PS}$=4.292, $C_{SW}$=103pF, $C_{CLAMP}$=200nF, $R_{CS}$=0.157Ω, $V_{CST}$=0.3V, and a single output capacitor with $R_{Co}$=20mΩ and $C_O$=600μF. The simulation conditions for $I_O$=0.1A and $I_O$=0.5A cases are $V_{BULK}$=375V, $V_O$=20V, and $N_{SW}$=4. The linear $S_{COMP}$ is designed equal to $S_F$ for $I_O$=0.5A, but the ratio between $S_{COMP}$ and $S_F$ becomes five times bigger for $I_O$=0.1A, so the dominate pole moves to 5 times lower frequency.

On the other hand, the nonlinear $S_{COMP}$ is designed with a 8μs time constant for $R_{COMP}$ and $C_{OSS(Qcomp)}$. The nonlinear ramp provides a shape slope ($S_{COMP}$=9·$S_{F(Io=0.5A)}$) in the first 8μs of every burst off time to improve noise immunity, and then $S_{COMP}$ flats out gradually afterward. This design behaves like $S_{COMP}$≈0 for $T_{BUR}$ > 24μs condition, so the dominate pole will not move to lower frequency for both 0.5A and 0.1A of $I_O$. As shown in Fig. 17, the nonlinear ramp design maintains a high gain over a wide load range, while the linear ramp is unable to hold.

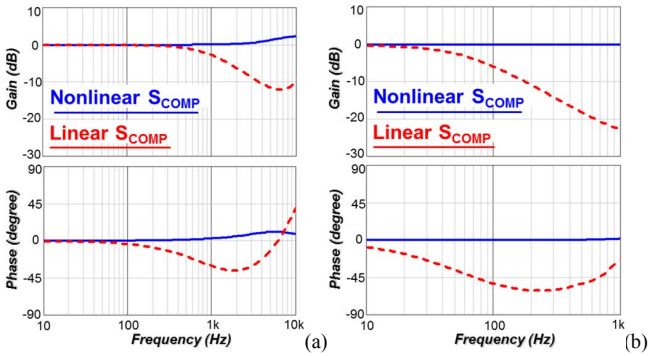


Fig. 17. Simulation comparison of $v_{REF}$-to-$v_{FB}$ transfer function for linear and nonlinear $S_{COMP}$ designs: (a) $I_O$=0.5A, (b) $I_O$=0.1A

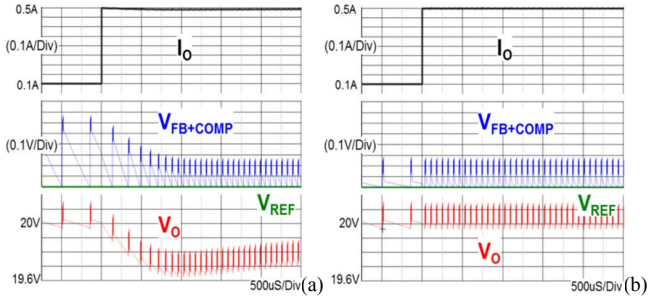


Fig. 18. Load transient simulation: (a) linear $S_{COMP}$, (b) nonlinear $S_{COMP}$

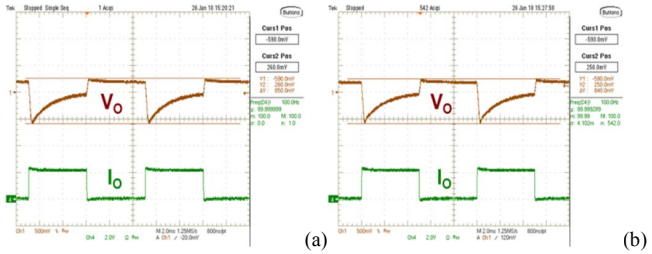


Fig. 19. Load transient test: (a) $V_{BULK}$=120V (b) $V_{BULK}$=325V

The time-domain load transient response of two $S_{COMP}$ designs is compared with the SIMPLIS simulations in Fig. 18. The results indicate that the burst loop with nonlinear $S_{COMP}$ responds to the step up load transient very quickly in one burst cycle, which verifies the conclusion from the frequency

domain in Fig. 17. The worst-case transient response of the GaN ACF hardware under a large repetitive step load change is shown in Fig. 19, which includes the dynamic response of both the ultra-fast burst mode design and the high-bandwidth transition mode. The test conditions for $V_{BULK}$=120V and 325V are $V_O$=20V, $I_O$ change between 0A and 2.25A, and 100Hz repetition rate. The peak-to-peak voltage spike is 800mV only, which is 4% of the 20V output.

## VI. CONCLUSION

Two new small-signal models for ACF in transient mode and burst mode are derived, and analytical compensation guides are developed in this paper. The transition mode model eliminates the need of deriving the resonant waveforms, and proves the benefit of a higher system control bandwidth than constant-frequency control. The model is further extended to ACF with a π output filter, and the parallel damping method is proposed to resolve the bandwidth limitation and minimize the full load efficiency compromise. Besides, the describing function method is applied to obtain an accurate burst mode model beyond the burst frequency, and the model is simplified to provide clear physical meaning. Two unique small-signal properties are discovered for the burst mode: the first is the insensitive loop stability to the ESR of the output capacitor compared with the conventional ripple control ($V^2$ control), while the second is the transient response impact of the additional ramp compensation in the burst control loop. After that, simple passive ripple compensation and a novel nonlinear ramp compensation are proposed to improve noise immunity and mitigate the tradeoff on transient response. Accuracy of the two proposed models is verified in SIMPLIS simulations. Finally, the ACF performance with proposed compensation methods are demonstrated on a high-density 45W GaN ACF adapter design.

## REFERENCES


[1] L. Xue and J. Zhang, "High efficient secondary-resonant active clamp flyback converter," *IEEE Trans. on industrial electronics*, vol. 65, no. 2, pp. 1235-1243, 2018.

[2] X. Huang, J. Feng, W. Du, F. Lee, and Q. Li, "Design consideration of MHz active clamp flyback converter with GaN devices for low power adapter Application," in *IEEE 2016 Applied Power Electronics Conference and Exposition (APEC)*, 2016, pp. 2334-2341.

[3] T. LaBella, B. York, C. Hutchens, and J. S. Lai, "Dead time optimization through loss analysis of an active-clamp flyback converter utilizing GaN devices," in *IEEE 2012 Energy Conversion Congress and Exposition (ECCE)*, 2012, pp. 3882-3889.

[4] R. PERRIN, N. Quentin, B. Allard, C. Martin, and M. Ali, "High temperature GaN active-clamp flyback converter with resonant operation mode," *IEEE Journal of Emerging and Selected Topics in Power Electronics*, no.99, pp.1-1, 2016.

[5] N. Quentin, R. Perrin, C. Martin, C. Joubert, B. Lacombe and C. Buttay, "GaN active-clamp flyback converter with resonant operation over a wide input voltage range," in *IEEE 2016 PCIM Europe*, 2016, pp. 1-8.

[6] L. Xue and J. Zhang, "Design considerations of high-efficient active clamp flyback converter using GaN power IC," in *IEEE 2018 Applied Power Electronics Conference and Exposition (APEC)*, 2018, pp. 777-782.

[7] Y. Yan, F. C. Lee, P. Mattavelli, "Unified three-terminal switch model for current mode controls," *IEEE Transactions on Power Electronics,* , vol.27, no.9, pp.4060-4070, Sept. 2012.

[8] P. Liu, "Demystifying active-clamp flyback loop compensation," training.TI.com, Oct. 2018.

[9] C. T. Choi, C. K. Li and S. K. Kok, "Modeling of an active clamp discontinuous conduction mode flyback converter under variation of operating conditions," in *IEEE 1999 Power Electronics and Drive Systems (PEDS)*, 1999, vol. 2, pp. 730-733.

[10] A. Bakkali, P. Alou, J. A. Oliver and J. A. Cobos, "Average modeling and analysis of a flyback with active clamp topology based on a very simple transformer," in *IEEE 2007 Applied Power Electronics Conference and Exposition (APEC)*, 2007, pp. 500-506.

[11] Min Chen and Jian Sun, "Reduced-order averaged modeling of active-clamp converters," *IEEE Transactions on Power Electronics*, vol. 21, no. 2, pp. 487-494, Mar. 2006.

[12] P. Liu, "Design consideration of active clamp flyback converter with highly nonlinear junction capacitance," in *IEEE 2018 Applied Power Electronics Conference and Exposition (APEC)*, 2018, pp. 783-790.

[13] J. Li and F. C. Lee, "Modeling of $V^2$ Current-Mode Control," *IEEE Trans, Circuits and Systems I*, vol.57, no.9, pp.2552-2563, Sept. 2010.

[14] S. Tian, F. C. Lee, Q. Li, and Y. Yan, "Unified equivalent circuit model and optimal design of $V^2$ controlled buck converters," *IEEE Trans. on Power Electronics*, vol. 31, no. 2, pp. 1734-1744, 2016.

[15] L. Huber, M. M. Jovanovic, "Small-signal analysis of DCM flyback converter in frequency-foldback mode of operation," in *IEEE 2013 Applied Power Electronics Conference and Exposition (APEC)*, 2013, pp. 1746-1752.

[16] D. Maksimovic, "Design of the zero-voltage-switching quasi-square-wave resonant switch," in *IEEE 1993 Power Electronics Specialists Conference (PESC)*, 1993, pp. 323-329.

[17] L. Xing, F. Feng and J. Sun, "Optimal Damping of EMI Filter Input Impedance," *IEEE Trans. on Industry Applications*, vol. 47, no. 3, pp. 1432-1440, May-June 2011.

[18] R.W. Erickson, "Optimal single resistor damping of input filters," in 1999 *Applied Power Electronics Conference and Exposition (APEC)*, 1999, pp. 1073–1079.

[19] J. Li and F. C. Lee, "New modeling approach and equivalent circuit representation for current-mode control," *IEEE Trans. on Power Electronics*, vol. 25, no. 5, pp. 1218-1230, 2010.